RMetS
Royal Meteorological Society

Estimating collision–coalescence rates from *in situ* observations of marine stratocumulus

Mikael K. Witte,[a]* Orlando Ayala,[b] Lian-Ping Wang,[c] Andreas Bott[d] and Patrick Y. Chuang[a]

[a]*Earth and Planetary Sciences, University of California Santa Cruz, Santa Cruz, USA*
[b]*Engineering Technology Department, Old Dominion University, Norfolk, VA, USA*
[c]*Department of Mechanical Engineering, University of Delaware, Newark, USA*
[d]*Meteorological Institute, University of Bonn, Germany*

*Correspondence to: M. K. Witte, National Center for Atmospheric Research, Boulder, CO, USA. E-mail: mkwitte@ucar.edu

Precipitation forms in warm clouds via collision–coalescence. This process is difficult to observe directly *in situ* and its implementation in numerical models is uncertain. We use aircraft observations of the drop-size distribution (DSD) near marine stratocumulus tops to estimate collision–coalescence rates. Marine stratocumulus is a useful system to study collisional growth because it is initiated near the cloud top and the clouds evolve slowly enough to obtain statistically useful data from aircraft. We compare rate constants estimated from observations with reference rate constants derived from a collision–coalescence box model, the result of which is termed the enhancement factor (EF). We evaluate two hydrodynamic collision–coalescence kernels, one quiescent and one including the effects of small-scale turbulence. Due to sampling volume limitations, DSDs must be averaged over length-scales much greater than those relevant to the underlying physics, such that we also examine the role of averaging length-scale with respect to process representation. Averaging length-scales of 1.5 and 30 km are used, corresponding roughly to the horizontal grid lengths of cloud-resolving models and high-resolution climate models, respectively. EF values range from 0.1 to 40, with the greatest EFs associated with small mode diameter cases and a generally decreasing trend with drop size. For any given drop size or averaging length-scale, there is about an order of magnitude variability in EFs. These results suggest that spatial variability on length-scales smaller than 1.5 km prevents accurate retrieval of rate constants from large-scale average DSDs. Large-scale models must therefore account for small-scale variability to represent cloud microphysical processes accurately. The turbulent kernel reduces EFs for all drop sizes, but can only account for at most half of the calculated EFs in marine stratocumulus.

Key Words: clouds; cloud microphysics; collision–coalescence; variability; precipitation

Received 24 January 2017; Revised 06 June 2017; Accepted 11 July 2017; Published online in Wiley Online Library 26 September 2017

1. Introduction

Low clouds such as trade cumulus and stratocumulus are often observed to precipitate, despite their muted dynamics in comparison with deep convection (Lau and Wu, 2003; Wood, 2012). In the absence of ice, collision–coalescence is the primary mechanism by which cloud droplets grow from the small sizes attainable by condensation alone (typically diameter $d < 30\,\mu$m) to become drizzle particles (diameter of order a few hundred μm), but the rate of growth of droplets of size $d \sim 20$–$50\,\mu$m is at a minimum with respect to both condensation and collision–coalescence, begging the question of how the first large drops are formed. This bottleneck in growth rate, often referred to as the 'warm rain problem' in the context of shallow cumulus, has garnered much attention in the cloud physics community over the years (e.g. Beard and Ochs, 1993).

Several solutions to explain the discrepancies between observations and numerical modelling results have been proposed, among which are the existence of ultragiant cloud condensation nuclei (Johnson, 1982; Jensen and Lee, 2008; Reiche and Lasher-Trapp, 2010), broadening of the drop-size spectrum due to turbulent mixing (Baker and Latham, 1979; Cooper *et al.*, 2013) and a direct role of turbulence in increasing collision rates (Wang and Grabowski, 2009). It is immensely challenging to observe collision–coalescence directly *in situ* because of limited instrument sampling volume and statistics, in addition to the near-impossibility of tracking individual drops in real time. Most observational studies attempting to quantify the collision–coalescence process took place in the laboratory during the mid-twentieth century (Hocking and Jonas, 1970; Shafrir and Gal-Chen, 1971; Davis, 1972; Jonas, 1972; Klett and Davis, 1973; Lin and Lee, 1975) and involved idealized experimental

configurations (e.g. bidisperse drops in quiescent conditions) that did not reproduce the complexity or turbulent nature of the atmosphere. Even modern-day direct numerical simulations of hydrometeors in incompressible turbulence, considered the gold standard for studies on the role of turbulence in drop-size evolution, are unable to reproduce the range of Reynolds numbers relevant to weakly turbulent stratocumulus (Ayala *et al.*, 2007).

Climate models are sensitive to the representation of clouds and precipitation because of their effects on the energy and moisture budgets of the atmosphere (Medeiros *et al.*, 2008). Clouds affect the planet's radiative budget by reflecting sunlight and modulating outgoing long-wave radiation and small changes in global cloud cover or albedo of just a few per cent could have a radiative forcing on par with that of anthropogenic greenhouse gas emission (Slingo, 1990). Precipitation affects numerous aspects of human life, as well as modulating cloud dynamics and lifetime; accurately predicting where and how much precipitation will fall to the surface remains a grand challenge in meteorology. Observational constraints on collision–coalescence rates are therefore needed to improve model prediction of cloud and precipitation amount as well as the spatio-temporal distribution.

Models represent cloud processes using several different approaches. The two most commonly used schemes assume that the size distribution of cloud particles either follows some fixed distribution (bulk schemes) or evolves freely (bin schemes), but the latter is much more computationally expensive. Bulk microphysical schemes employed in large-scale models use a threshold size (typically $d \sim 40–50\,\mu\text{m}$) to divide liquid water drops into 'cloud droplet' and 'raindrop' categories such that the collision–coalescence process is subdivided into three regimes: autoconversion (production of raindrops by collisions of cloud drops), accretion (growth of raindrops by scavenging of cloud drops) and hydrometeor self-collection (growth of raindrops by collisions with other raindrops).

Austin *et al.* (1995) analyzed aircraft observations of the drop-size distribution (DSD) taken off the coast of California to estimate the autoconversion rates necessary to reproduce observed precipitation rates, using an equilibrium model that also took into account the effects of condensation, accretion, sedimentation and turbulent mixing. For a precipitation-producing DSD, the authors found that autoconversion rates two orders of magnitude greater than predicted were required to match the observed precipitation flux (Austin *et al.*, 1995).

There are several factors that may contribute to such large discrepancies. For example, the cloud microphysical measurements were performed using a Forward Scattering Spectrometer Probe (FSSP), which is known to overcount large drops and undercount small drops, due to coincidence of small drops in the instrument view volume (Chuang *et al.*, 2008); this may have resulted in overestimation of autoconversion rates given the observed DSDs. In addition, only three 60 s average spectra were analyzed by Austin *et al.* (1995) and the shape and concentration of the DSD in the autoconversion regime were held constant throughout the depth of the modelled cloud. These assumptions preclude the effects of vertical development of the DSD, in particular the assumption of constant DSD shape. *In situ* observations of stratocumulus show an increase in DSD mode diameter with increasing height due to condensation, while a widening of the right tail of the DSD is observed when descending from the cloud top, due to collision–coalescence (Rossiter, 2012). From the modelling perspective, Igel and van den Heever (2017) simulate shallow cumulus fields using a cloud-resolving model with bin microphysics and find that estimated DSD shape parameters are highly variable in both the horizontal and vertical dimensions.

A result qualitatively similar to that of Austin *et al.* (1995) was found by Pincus and Klein (2000) in their analysis of the 'tuning parameters' used to modulate autoconversion rates in large-scale models, where rate enhancements of up to a factor of 15 are needed to reach agreement with observations. Pincus and Klein (2000) attribute the cause of autoconversion rate underprediction to subgrid-scale variability in the quantities used to calculate process rates, such as vertical velocity or liquid water mixing ratio, and the nonlinear relationship between those quantities and process rates. This insight led to the development of statistical 'upscaling' schemes that integrate over an assumed probability density function of subgrid-scale variability to predict process rates more accurately (e.g. Morrison and Gettelman, 2008; Larson and Griffin, 2013). Despite such advances in representing the effects of small-scale variability, the definition of a 'local' length-scale with respect to the drop-size distribution remains ill-defined; a recent review of microphysical process parametrizations suggested 100 m as sufficient (Khain *et al.*, 2015), but this value was derived from modelling studies and has not been evaluated observationally.

In this study, we seek to retrieve collision rates in the bottleneck size regime ($d \sim 20–50\,\mu\text{m}$) from *in situ* aircraft observations of stratocumulus and explore the role of spatial variability in the DSD in controlling retrieved rates. In particular, we focus on the first few collisions that drops undergo, by using observations of the stratocumulus cloud-top region where drizzle is initiated (Vali *et al.*, 1998; Stevens *et al.*, 2003). The analysis is applied to observations averaged over two length-scales: the length of an entire observational leg (∼30 km) and a single penetration through the cloud top (∼1.5 km). These length-scales correspond roughly to the horizontal grid size of the highest-resolution climate models (tens of km; see table 9.1 in Haarsma *et al.*, 2016) and the resolution of a typical cloud-resolving model (∼1 km, e.g. Blossey *et al.*, 2007), respectively.

2. Method

2.1. Observations

We use observations from the Physics of Stratocumulus Top (POST) flight campaign, which took place during July and August 2008 off the central California coast. Flights were conducted by the Center for Interdisciplinary Remotely Piloted Aircraft Studies (CIRPAS) Twin Otter aircraft with dynamic, thermodynamic and microphysics instrumentation (details available in Carman *et al.*, 2012 and Gerber *et al.*, 2013). The flight plans were designed to follow approximately a Lagrangian air mass, while sampling the interface between the stratocumulus layer and the free troposphere in the vertical direction (Malinowski *et al.*, 2013). To this end, the Twin Otter primarily sampled the cloud top region in a sawtooth pattern, repeatedly ascending and descending from ∼100 m below cloud top to ∼100 m above at a vertical rate of change of $\sim 1.5\,\text{m}\,\text{s}^{-1}$. Each leg was composed of 4–5 sawtooth manoeuvres that took about 10 min total and covered roughly 30 km. We refer to the individual ascents and descents of each leg as 'segments' and will use these segments as the smallest sampling unit in our analyses. In between the cloud-top legs, surface and below-cloud flux legs were executed as well as at least one vertical sounding at the beginning and/or end of each flight.

There were 17 research flights flown during POST that sampled a range of meteorological and microphysical conditions, inversion strength, rain rate, aerosol loading, time of day, etc. (cf. Table 1 herein and table 1 of Gerber *et al.*, 2013). All flights are considered in this study except TO9, because the observed cloud layers were too low and thin to yield adequate cloud observations, resulting in a total of 51 flight legs for analysis. We use 1 Hz cloud drop-size distributions (DSDs) inferred from an Artium Flight Phase Doppler Interferometer (PDI: Chuang *et al.*, 2008), which measures drops up to diameter $d \sim 200\,\mu\text{m}$. The Twin Otter was also equipped with a Droplet Measurement Technologies Cloud Imaging Probe (CIP) that samples drops of diameter 25–1550 μm. We convert from number to mass concentration assuming spherical drops and calculate liquid water content (LWC) as well as sedimentation flux (or rain rate R) by integrating over the PDI distributions. This method of calculating LWC compares

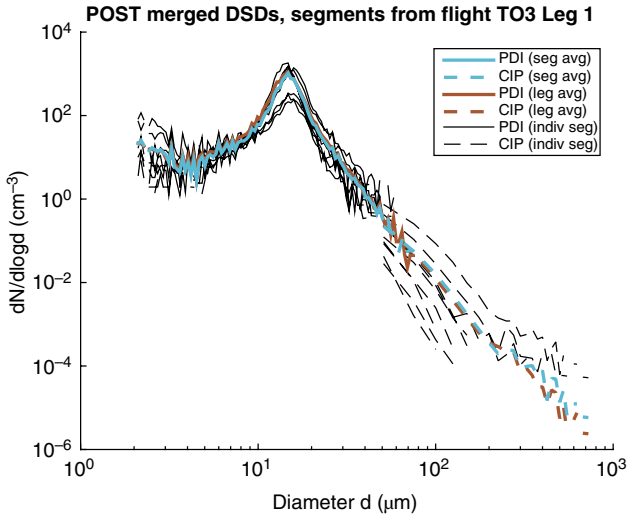

Figure 1. Typical DSD observations from both cloud probes on the CIRPAS Twin Otter (PDI and CIP) from TO3 Leg 1. Despite the relative smoothness of the leg composite DSD for $d > 10\,\mu$m (average over 30 km), note the variability in the segment DSDs (averaged over 1.5 km, thin black traces). There is an overlap size region in which both instruments measure (25–100 μm; first CIP bin measuring drops smaller than 50 μm is not shown). In the mean, these observations overlap but this is not true of most individual segments. Discontinuities are due primarily to the low probability of observing 'large' drops in the PDI view volume. [Colour figure can be viewed at wileyonlinelibrary.com].

well with the Twin Otter standard Gerber PVM-100A LWC after accounting for differences in drop size range measured (Carman *et al.*, 2012). LWC is used to identify cloud-top height z_{CT}, here defined as the highest altitude with median LWC $> 0.05\,\mathrm{g\,m^{-3}}$ during a given leg. Cloud-top rain rate R_{CT} is derived from leg composite merged DSDs (i.e. combined PDI and CIP data) with an instrument crossover diameter at $d_{cross} = 64\,\mu$m.

For the analysis, the drop-size distribution within 40 m of the estimated cloud-top height is averaged to give a leg composite mean DSD, which we assume is representative of the mean cloud state. The mode diameter is used as the characteristic size of the leg composite mean DSD; this is a reasonable measure to use because cloud-top DSDs typically exhibit a single peak in number concentration (Figure 1). Examination of leg mode diameter d_0 in Table 1 shows minimal variability among legs (typically d_0 varies by <2 μm per flight, corresponding to about one PDI bin) but substantial variability among days (d_0 ranges from 12.8 to 30.3 μm). Each segment can also be analyzed individually, thus reducing the averaging distance from 30 to ∼1.5 km. Individual segments were subject to slightly different criteria to be included in the analysis: we require segment mean $LWC > 0.05\,\mathrm{g\,m^{-3}}$ and mean total drop number concentration $N_D > 5\,\mathrm{cm^{-3}}$. An alternate leg composite DSD can then be calculated by taking the mean over the individual segment DSDs from a given leg. The effects of using this alternate composite are explored in section 3.2.3. As might be expected, there is somewhat more variability in d_0 when derived from segments than from the standard leg composite, with six of 51 legs exhibiting a standard deviation in segment d_0 greater than 3 μm. This is due mostly to using the mode statistic for the characteristic size.

2.2. *Rebinning of the DSD*

Drop-size distributions near the cloud top typically exhibit a single peak, followed by a rapid decrease in concentration on either side of the peak as measured by both the PDI and CIP. An example DSD is shown in Figure 1. For POST DSDs, the PDI accurately counts drops up to 50–75 μm in diameter depending on the case, above which the sampling volume is insufficient for robust drop-counting statistics. Heavily drizzling cases (i.e. cases with more large particles) have a broader usable sampling range for both cloud probes, while for non-drizzling cases very few drops greater than $d \sim 100\,\mu$m are observed. As 50 μm is a widely accepted threshold diameter for efficient drop growth by collision–coalescence (Pruppacher and Klett, 2010), the drop-size regime sampled by the PDI is ideal for investigating the onset of the collision–coalescence process.

In order to examine more closely the first few collisions drops undergo and the rates at which these collisions occur, we take the approach proposed by Rossiter (2012) and rebin the DSD in terms of the number of collisions a drop has experienced. The mode diameter of a DSD is assumed to be the mean monomer size. We use the term 'monomer' to describe the basic unit of mass m_0 formed by condensation, from which larger drops are formed by collisions. It is comparable to the concept of an 'embryonic drizzle drop' (e.g. Wood *et al.*, 2009b), except that in this study we seek to examine the rate of formation of 'embryonic drizzle' via collisions of monomers.

The DSD rebinning proceeds in integer multiples of the monomer mass such that bin i is centred at $m_i = (m_0, 2m_0, \ldots, (I+1)m_0)$ for $i = (0, 1, \ldots, I)$. Bin boundaries lie halfway between the integer masses, i.e. bin i covers $[(i+\frac{1}{2})m_0, (i+\frac{3}{2})m_0)$. In this analysis, we assume that (i) an input DSD can be interpreted as the steady-state distribution representative of the mean state of the cloud-top region; (ii) drops substantially smaller than the mode diameter are assumed to grow by condensation alone; (iii) drops substantially larger than the mode diameter grow by collision–coalescence alone; and (iv) all collisions involve a monomer-size drop. Sedimentation, evaporation due to entrainment mixing and drop breakup are neglected. The drops considered here ($d < 100\,\mu$m) are too small for breakup to be important. The validity of these assumptions will be evaluated in sections 3.1.2 and 3.2.4.

2.3. *Estimating rate constants from a DSD*

A simplified equation for the early stages of collisional drop growth can be given by

$$\frac{\mathrm{d}n_j}{\mathrm{d}t} = k_{j-1} n_0 n_{j-1} - k_j n_0 n_j \qquad (1)$$

for $j = 1, 2, \ldots, J$, where n_j is the concentration of drops in the jth bin, k_j is the rate constant for collisions between monomers and drops in bin j and J is the total number of collisions to be analyzed. The monomer concentration n_0 is known, but the rate constant k_0 is not. This equation excludes collisions between non-monomers, an assumption we will test below. When applied to observations, we assume the drop-size distribution is at a steady state such that $\mathrm{d}n_j/\mathrm{d}t = 0$. This results in a linear system of J equations with $J+1$ unknowns: $(k_0, k_1, \ldots, k_J)$. To close the system with respect to the observations, we specify k_0, which can be interpreted as a source term to replenish monomers lost by collision. Further details about the analytical framework are described in Appendix A.

It is important to stress that we have intentionally chosen the term 'rate constant' rather than 'collision kernel' to describe the unknowns k_j. This is because (i) we have (by assumption) neglected non-monomer collision possibilities in order to reduce the number of closure parameters necessary, (ii) the kernel depends fundamentally on local concentrations but the rate constant analysis is applied to observed DSDs averaged over ones to tens of kilometres and (iii) conceptually, the quantity is framed more accurately by the 'rate constant' terminology with which chemists are familiar: it depends solely on number concentrations without reference to any physical mechanism, while the collision kernel is rooted in the physics of the collision–coalescence process.

3. Results

In this study, we seek to understand observations of the DSD in the context of existing collision kernels. The final goal is to

Table 1. Microphysical characteristics of POST flights calculated from top 40 m of cloud. All values represent the mean over a 30 km flight leg and the order of values corresponds to the leg number. Cloud-top z_{CT}, monomer diameter d_0, total concentration N_D and power-law slope parameter β are calculated from the PDI only. Cloud-top rain rate R_{CT} is calculated from both the PDI and CIP instruments. Refer to the text for more details on how each quantity is computed.

Flight #	Date	z_{CT} (m)	d_0 (μm)	N_D (cm^{-3})	β	R_{CT} (mm day^{-1})
TO1	2008-07-16	505, 515, 515	18.3, 18.3, 18.3	128, 116, 149	3.87, 3.84, 3.70	0.56, 0.46, 0.56
TO2	2008-07-17	505, 515, 465	18.3, 18.3, 14.7	91, 110, 110	3.60, 3.44, 3.28	0.30, 0.40, 0.24
TO3	2008-07-19	455, 475, 455	14.7, 14.7, 14.7	159, 201, 242	3.18, 3.22, 3.20	0.28, 0.37, 0.45
TO4	2008-07-21	975, 955, 925	26.2, 26.2, 24.4	46, 53, 37	3.92, 3.79, 3.36	0.73, 1.00, 0.79
TO5	2008-07-28	426, 415, 505	17.0, 18.3, 18.3	59, 82, 93	3.79, 3.86, 3.79	0.15, 0.28, 0.33
TO6	2008-07-29	655, 585, 535	18.3, 18.3, 18.3	165, 144, 137	4.06, 3.90, 3.85	0.60, 0.44, 0.37
TO7	2008-07-30	325, 345, 315, 365	28.2, 24.4, 24.4, 24.4	27, 24, 28, 34	3.72, 3.29, 3.18, 3.50	0.70, 0.61, 0.63, 0.59
TO8	2008-08-01	365, 385, 425, 285	24.4, 21.1, 30.3, 21.1	19, 17, 15, 38	2.82, 1.95, 3.87, 2.79	0.59, 0.55, 0.63, 0.42
TO10	2008-08-04	633, 645, 585	18.3, 18.3, 14.7	130, 106, 100	3.29, 3.29, 2.72	0.64, 0.54, 0.39
TO11	2008-08-06	496, 575, 555, 515	12.8, 14.7, 12.8, 12.8	74, 114, 115, 112	3.30, 4.20, 3.75, 3.57	0.07, 0.10, 0.11, 0.11
TO12	2008-08-08	704, 725, 685	16.4, 17.0, 16.4	104, 118, 123	4.20, 4.26, 4.13	0.24, 0.31, 0.24
TO13	2008-08-09	555, 605, 635	28.2, 28.2, 26.2	26, 29, 32	3.81, 3.81, 4.23	1.08, 0.95, 1.09
TO14	2008-08-12	495, 495, 495	24.4, 24.4, 24.4	65, 78, 55	3.93, 3.98, 3.98	1.02, 1.14, 0.95
TO15	2008-08-13	415, 435, 475	18.3, 17.0, 18.3	55, 80, 79	2.87, 3.04, 2.88	0.36, 0.38, 0.63
TO16	2008-08-14	395, 435, 425	22.7, 22.7, 21.9	59, 54, 62	4.12, 3.91, 3.93	0.61, 0.59, 0.62
TO17	2008-08-15	415, 405, 435	21.1, 21.1, 21.1	86, 68, 70	4.03, 3.85, 3.69	0.67, 0.40, 0.53

evaluate how well observed collision rates compare with those predicted by a model using known kernels. The remainder of the section is organized as follows.

(1) A collision–coalescence box model is used to generate 'reference' rate constants (section 3.1).
   - Assumes collision–coalescence is the only process modifying the DSD.
   - Two different hydrodynamical kernels are used to generate reference rate constants, including one that accounts for the effects of small-scale turbulence.
   - Box model predictions are generated using observed, spatially averaged DSDs as initial conditions.

(2) The rate constant framework (Eq. (1)) is then used to generate the collision rates necessary to maintain a steady state, termed the 'observed' rate constants (section 3.2).
   - Rate constants are determined using the same observed, spatially averaged DSDs as in section 3.1.
   - A steady state is assumed. In reality, it is possible that the actual collision rates relevant to the first few collisions are faster (when a cloud is developing) or slower (when a cloud is dissipating). The steady state is therefore not an extreme assumption in either direction.
   - We report our results as a ratio between 'observed' and 'reference' rate constants, the result of which is termed the 'enhancement factor.'

3.1. *Reference rate constants from a box model*

3.1.1. *Description of the model*

Before applying the rate constant analysis to observations, we characterize the rate constant using known DSDs and collision rates. We use the zero-dimensional (i.e. no spatial dependence) collisional growth model of Bott (1998) (hereafter referred to as the Bott or box model) to derive reference rate constants and compare various formulations of the collision kernel. The initial DSD closely matches the observations: for drops of $m < 1.5m_0$, the distribution is log-normal centred at d_0 with geometric standard deviation $\sigma = 1.2$; drops with $m \geq 1.5m_0$ follow a power law with slope parameter β as fit to the observations. The model was run for each observed pair of d_0 and β with all collisions allowed (i.e. including collisions between non-monomers).

For later comparison with theory and observations, the model was run with two different collision kernels: the Hall and Ayala hydrodynamical collision kernels (Hall, 1980; Ayala *et al.*, 2008). The Hall kernel assumes quiescent background flow, while the Ayala kernel accounts for small-scale turbulence effects on collision efficiency, radial relative velocity and a clustering coefficient that describes deviations from a uniform random spatial distribution. As in Wyszogrodzki *et al.* (2013), these effects are parametrized as nonlinear functions of the turbulent energy dissipation rate ϵ using the geometric collision kernel and clustering coefficients of Ayala *et al.* (2008) and turbulent collision efficiencies from Wang and Grabowski (2009). Collision efficiencies are defined explicitly from DNS results for $\epsilon = \{100, 400\}$ cm^2 s^{-3} as a multiplicative factor applied to Hall kernel collision efficiencies; efficiencies for other values of ϵ are calculated by linear interpolation. At the lower limit of quiescence, the Ayala kernel reduces to the Hall kernel. Here, the Ayala kernel is calculated for discrete values of dissipation rate relevant to shallow clouds, $\epsilon = \{3, 10, 30, 100, 300\}$ cm^2 s^{-3}.

3.1.2. *Reference rate constants*

The Bott model gives the drop concentration as a function of time and drop size. Rate constants are calculated from the drop-size distribution at the end of each Bott model run using a variant of Eq.(1) (see Appendix A for details). The parameter k_0 is calculated explicitly, as the change in monomer concentration with time dn_0/dt is known. The relative differences in concentration n_j over a single time step (i.e. $(n_j(\Delta t) - n_j(0))/n_j(0)$) are typically less than 1% and never exceed 7%. Computed rate constants from all POST legs using the Hall kernel are shown in Figure 2 as a function of 'collector drop' diameter D, where $D = d_0(j+1)^{1/3}$.

Rate constants are lowest for the first collision and increase significantly (by 2–4 orders of magnitude) with collector drop size. This is expected, because kernel values are at a minimum for collisions of similar size drops due to low relative velocity. In addition, the maximum rate constant magnitude for a given DSD correlates positively with monomer size (indicated by trace shading) and negatively with slope parameter (not shown). Results using the largest calculated kernel values (Ayala kernel with $\epsilon = 300$ cm^2 s^{-3}, hereafter A300) are about 13 times greater than the Hall rate constants for the smallest monomer case and decrease nearly monotonically with d_0 to about a factor of 2 greater for the largest monomer cases (see inset in Figure 2). This is expected, because smaller drops are impacted by turbulence effects more strongly than larger drops due to their lower mass, such that smaller drops are more easily perturbed from gravitational trajectories. Rate constants using the Ayala kernel at intermediate dissipation rates ($0 < \epsilon < 300$ cm^2 s^{-3}) display similar behaviour, with rate constants that fall in between the slowest and fastest kernels (Hall and A300, respectively).

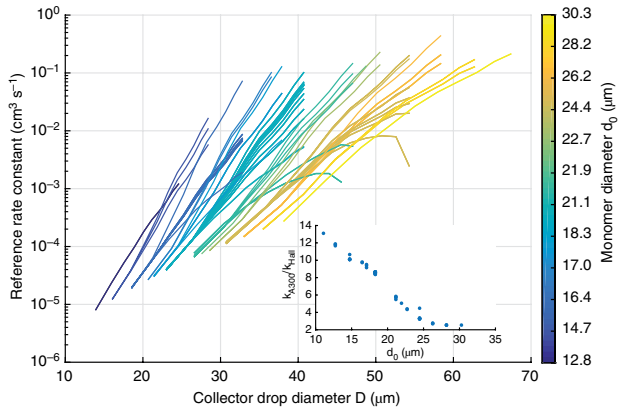

Figure 2. Reference rate constant as a function of collector drop diameter from the Bott model using the Hall kernel. Line shading is by monomer diameter, showing a strong relationship between monomer size and rate constant. The inset shows the ratio of rate constants derived using A300 versus the Hall kernel as a function of monomer diameter. [Colour figure can be viewed at wileyonlinelibrary.com].

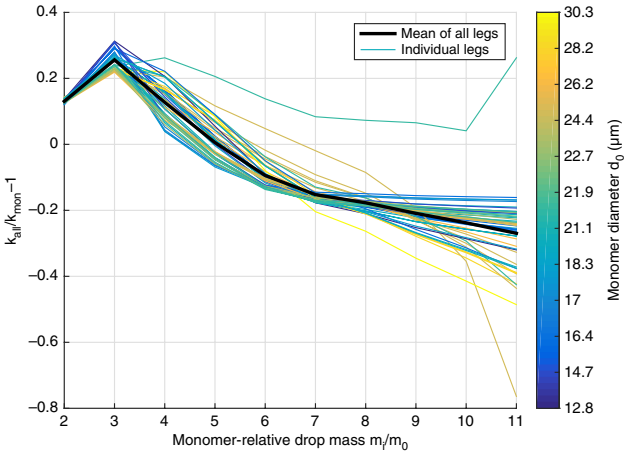

Figure 3. Comparison of reference rate constants calculated from Bott model output in which all collisions are allowed (k_{all}) and only collisions with monomers are allowed (k_{mon}). The difference in reference rate constants relative to k_{mon} is shown as a function of monomer-relative drop mass. Data were generated using the Hall kernel. [Colour figure can be viewed at wileyonlinelibrary.com].

3.1.3. *How important are non-monomer collisions?*

The contribution of collisions of non-monomers to changes in concentration in the analyzed size range must also be considered. The Bott model was run with only monomer collisions permitted (k_{mon}) and the resulting rate constants were compared with the 'all collision' model output (k_{all}), as shown in Figure 3. The k_{mon} values were computed using the same method as for k_{all} (i.e. Eq. (A1) with $\Delta i = [0, 1, 2]$), such that any differences between k_{all} and k_{mon} are only a result of altering Bott model physics.

Allowing non-monomer collisions affects rate constants as a function of monomer-relative drop mass m_i/m_0, where the subscript i is related to the number of monomer collisions j by $j = i - 1$. For the first few collisions ($m_i/m_0 < 4$), $k_{all} > k_{mon}$, but for collector drops much larger than monomers, non-monomer collisions exert a greater influence such that $k_{all} < k_{mon}$. The consistency in the pattern of each trace in Figure 3 arises from how collision efficiency is calculated using the Hall and Ayala kernels: it depends on the monomer-collector drop-size ratio as well as the size of the collector drop and the abscissa of Figure 3 shows constant monomer-collector drop-size ratios. Despite this pattern, Figure 3 shows that monomers are the dominant contributor to reference rate constants, as evidenced by the fact that the relative difference between k_{all} and k_{mon} is less than 50% for all but one of the analyzed DSDs. Differences between k_{all} and k_{mon} for the Ayala kernel exhibit a similar pattern: a pronounced maximum at $m_i/m_0 = 3$ followed by a decrease to about -0.2 at greater drop-size differential. Self-collisions between drops of size $m_i/m_0 = 2$ are increasingly important at higher dissipation rates, such that the peak at $m_i/m_0 = 3$ increases with turbulence intensity, especially for small monomer cases ($d_0 \lesssim 18\,\mu$m). At the highest dissipation rate examined ($\epsilon = 300\,\text{cm}^2\,\text{s}^{-3}$), $k_{all}/k_{mon} \sim 2$ at $m_i/m_0 = 3$. Otherwise, the shape and magnitude of the comparison is similar across the range of dissipation rates used ($0 \leq \epsilon \leq 300\,\text{cm}^2\,\text{s}^{-3}$) and Ayala kernel results are therefore not shown. Given the dynamic range of reference rate constants, a relative error of up to approximately a factor of 2 is acceptable and the 'all collision' reference rate constants are used in the calculation of enhancement factors.

In the Bott model, collision–coalescence is the only process modifying the drop-size distribution. The reference rate constants calculated from model output transform a theoretically derived collision kernel into an observable quantity, with no added uncertainty due to other physical processes. Therefore, when the rate-constant analysis is applied to the observations, we will scale the results by the Bott model output to compare observed rate constants with the reference rate constants derived from the Bott model. This allows us to evaluate quantitatively the rate of collision–coalescence in shaping observed DSDs.

3.2. *Rate constants from observations*

3.2.1. *Closure assumption*

When applying rate-constant analysis to observations of the cloud-top DSD, we define the closure parameter k_0 as the monomer source rate balancing the loss of drops to higher bins. We interpret this as the vertical rate of advection of monomers to the cloud-top region. Given a mean updraught velocity $\overline{w_\uparrow}$ and updraught fraction $f_\uparrow$ (updraughts are defined as $w > 0.01\,m\,s^{-1}$) and a cloud-top layer of thickness h and mean monomer concentration n_0 just below the cloud-top layer, the monomer source rate is given by $k_0 = (f_\uparrow \overline{w_\uparrow})/(n_0 h)$. A cloud-top layer of thickness 40 m is chosen. The mean updraught velocity, updraught fraction and n_0 were diagnosed using data from 40 to 80 m below the cloud top to calculate leg-specific k_0 values, which range from 1.2×10^{-5} cm^3 s^{-1} to 1.3×10^{-4} cm^3 s^{-1}, with a mean of 3.8×10^{-5} cm^3 s^{-1}.

3.2.2. *Observed rate constants and enhancement factors from leg composites*

Observed rate constants from DSDs averaged over 30 km legs are shown in Figure 4. Rate constants increase with increasing collector diameter. The magnitude of the rate constants generally increases with monomer size (shading of traces in Figure 4), although this size sorting is not perfect. Such sorting is expected, because larger monomers collide more effectively, all else being equal (i.e. no change in number concentration, kernel values, etc.).

We define the enhancement factor (EF) to be the ratio of the observed rate constants relative to the reference rate constants calculated from the Bott model output. If the sampled volume is uniform (homogeneous DSD) and the kernel represents collision–coalescence in the atmosphere accurately, then we expect the EF to be unity. Deviations from unity may be caused by processes unaccounted for in the Bott model (most notably condensation/evaporation and sedimentation), errors in kernel formulation or spatial heterogeneity in the DSD. EFs with respect to the Hall kernel are shown in Figure 5, with values ranging from 0.1 to 40. EF is inversely related to monomer size and some of the large monomer cases exhibit values less than unity.

Correlation tests were performed for enhancement factor and leg-mean liquid water content, rain rate, adiabaticity and turbulent dissipation rate. No statistically significant correlation was found between any of these quantities and enhancement factor. One leading explanation for EF greater than unity is spatial variability in the DSD. Spatial averaging of *in situ* DSD

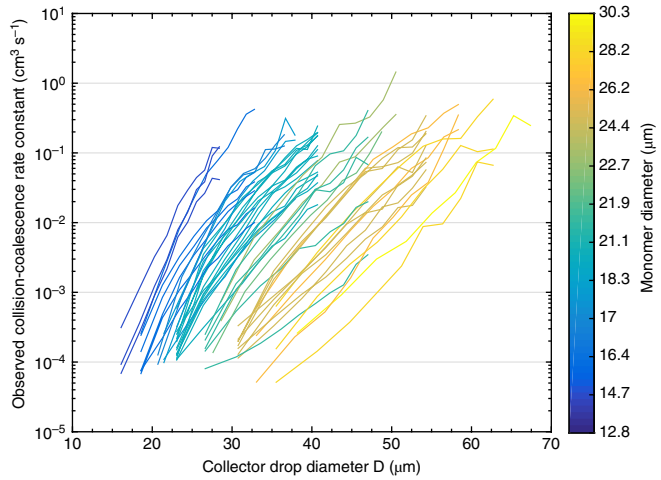

Figure 4. Rate constants as calculated from POST PDI observations. [Colour figure can be viewed at wileyonlinelibrary.com].

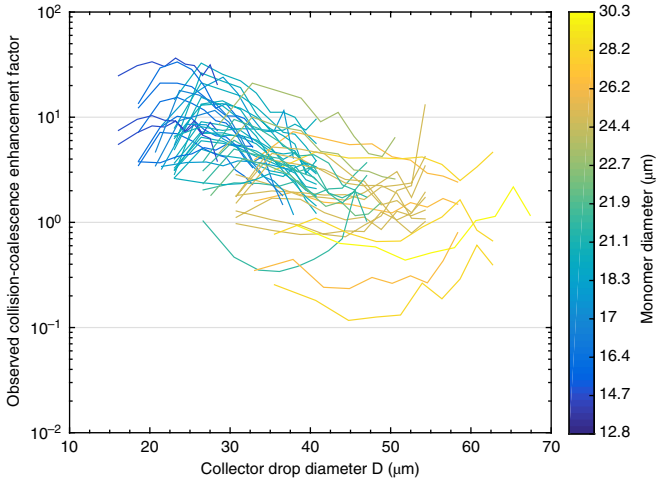

Figure 5. Observed rate constants relative to reference rate constants calculated using the Hall kernel. [Colour figure can be viewed at wileyonlinelibrary.com].

observations has been shown to result in broader distributions (Geoffroy *et al.*, 2010). A broader DSD will result in greater rate constants, because more large drops must be produced faster. The notion that a smaller DSD averaging length-scale leads to reduced rate constants and enhancement factors will be explored further in the following section.

3.2.3. *Enhancement factors from individual segments*

The leg composite DSD averages used in the previous section were calculated from 8 to 10 discontinuous segments. Each of these cloud-top segments was about 1.5 km in length for a total of 30 km sampled per leg, which includes time spent above cloud and below the cloud top. We now perform the same analysis over each 1.5 km segment to resolve smaller scale heterogeneity in the DSD. Counting statistics preclude analyses at averaging lengths much shorter than this. Segments with mean $LWC < 0.05\,\mathrm{g\,m^{-3}}$, $N_\mathrm{D} < 5\,\mathrm{cm^{-3}}$ or maximum drop size sampled $m_\mathrm{max} < 8m_0$ are excluded, for a total of 303 usable segments out of 449 total segments from 51 flight legs. Not surprisingly, the population of 303 segments exhibits greater variability than the 51 leg averages in nearly all relevant characteristics of the DSD, e.g. total concentration, mode diameter and DSD shape parameter β.

Rate constants and enhancement factors are calculated from segments using leg composite k_0 values. Figure 6 shows PDFs of enhancement factor relative to the Hall kernel conditioned on collector drop diameter (i.e. Figure 6 does not present a joint PDF; instead each column sums to unity). Segment mean EFs exhibit

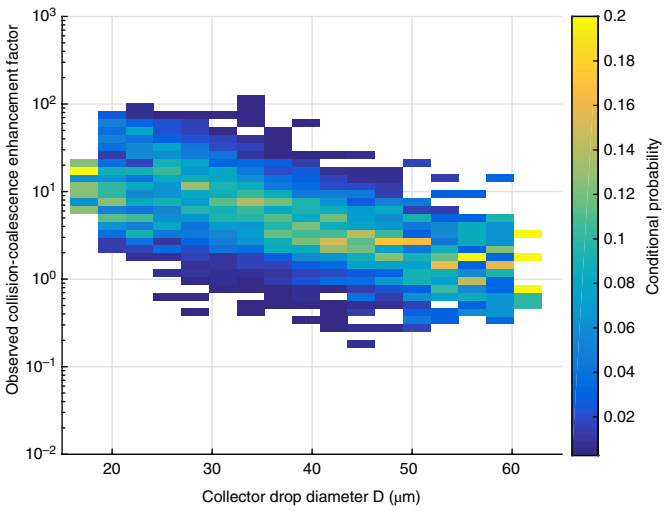

Figure 6. Probability density functions of enhancement factor relative to the Hall kernel from segments, conditioned on collector drop diameter. [Colour figure can be viewed at wileyonlinelibrary.com].

a slightly broader range of values (0.2–111) than leg composite EFs (cf. Figure 5), with most of the increase in variability at intermediate collector drop diameters ($30 < D < 40\,\mu\mathrm{m}$). Results from both leg composites and individual segments generally display 1–2 orders of magnitude of variability in EF, suggesting that an average over 1.5 km remains too coarse a spatial resolution to describe collision–coalescence accurately. It is possible that using leg composite k_0 values partly contributes to the wider range of EF in Figure 6.

3.2.4. *Sensitivity of results to process representation*

Enhancement factors from leg mean DSDs using the Ayala kernel with $\epsilon = 30\,\mathrm{cm^2\,s^{-3}}$ (hereafter referred to as the A30 kernel) are shown in Figure 7. This value of ϵ represents an upper bound on the effects of turbulence on collision–coalescence in marine stratocumulus, where the mean ϵ is typically of the order of $10\,\mathrm{cm^2\,s^{-3}}$ (Siebert *et al.*, 2010). EFs are lower across the board than in Figure 5, ranging from 8×10^{-2} to 19. Overall, enhancement factors decrease by approximately a factor of 2 compared with Hall kernel results. Size sorting occurs for A30 EF values relative to Hall kernel results, such that the greatest difference in EF is obtained for monomer cases with $d_0 \sim 15\,\mu\mathrm{m}$. The difference between A30 and Hall EF decreases with monomer size; the largest monomer case ($d_0 = 30.3\,\mu\mathrm{m}$) exhibits an EF only about 1.6 times smaller than the corresponding Hall kernel results. It is notable that the EF remains of the order of 10 for several small- to intermediate-sized monomer cases ($d_0 \lesssim 20\,\mu\mathrm{m}$), suggesting that turbulence alone cannot explain enhancement factors greater than unity.

Austin *et al.* (1995) performed a similar study in which they estimated autoconversion rates (i.e. non-size-resolved collision rates) from observations of marine stratocumulus. They found that autoconversion enhancements of 'almost two orders of magnitude' were necessary to reproduce observed precipitation fluxes over an averaging length $L \approx 18\,\mathrm{km}$. The results presented here are qualitatively in agreement with their previously reported figures, insofar as enhancement factors generally exceed unity, but we find that EFs relative to the quiescent Hall kernel are generally of order 10 and decrease with monomer size, collector drop size and turbulence intensity (i.e. dissipation rate).

Unlike the idealized analytical framework developed here, clouds in nature are never in a steady state and collision–coalescence does not occur in temporal isolation; rather it occurs simultaneously and continuously with the other microphysical processes affecting the evolution of the DSD.

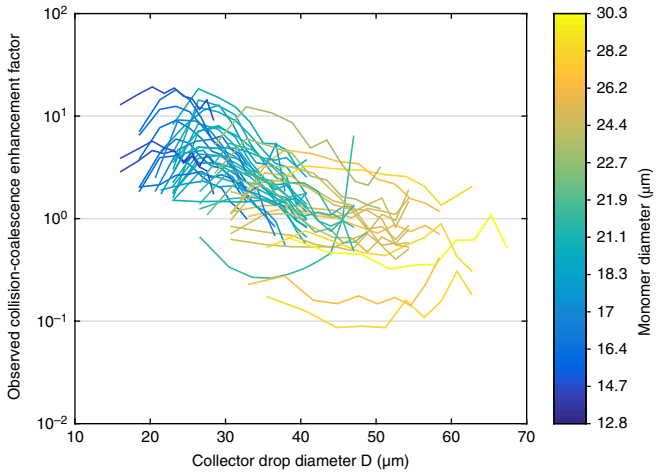

Figure 7. Observed rate constants relative to reference rate constants calculated using the Ayala kernel with $\epsilon = 30\,\mathrm{cm^2\,s^{-3}}$. Compared with Figure 5, EF values associated with small monomer legs decrease more than larger monomer cases, in agreement with the inset of Figure 2. [Colour figure can be viewed at wileyonlinelibrary.com].

Small variations in radiative cooling, entrainment and in-cloud turbulence cause inhomogeneities that are not resolved at kilometre length-scales that ostensibly allow populations of drops with different histories to interact, perhaps thus increasing the efficacy of collision–coalescence in a manner that we are not presently able to resolve in the observations. For example, de Lozar and Muessle (2016) use direct numerical simulations of a cloudy mixed layer to show that a small number (<1%) of droplets at the cloud top can grow to twice the monomer mass via condensation alone by decoupling from large-scale convective eddies.

The rate constants and enhancement factors presented here should be viewed as lower bounds on actual values, despite our neglect of other microphysical processes. Inclusion of drop loss processes such as evaporation and sedimentation would serve to increase rate constants, because of the steady-state assumption: an increase in the rate of drop loss from a bin must be compensated by a commensurate increase in the collisional production rate and therefore rate constants. Mass-weighted sedimentation flux was added to the steady-state system of equations to examine the quantitative impact of neglecting this process. Sedimentation increased the resulting rate constants by at most a few per cent. This should not come as a great surprise; the largest drops considered in the analysis ($d \sim 65\,\mu\mathrm{m}$) have a sedimentation velocity of order $10\,\mathrm{cm\,s^{-1}}$.

4. Discussion and summary

The results presented in this study generalize the warm rain problem: not only do models have trouble producing precipitation on observed time-scales in shallow cumulus, but observationally derived rate constants cannot be accurately recovered from a collision–coalescence box model even in the lightly or non-precipitating marine stratocumulus sampled during POST.

Aircraft *in situ* observations of the cloud drop-size distribution from the POST field campaign were analyzed to retrieve effective collision–coalescence rate constants in marine stratocumulus. We use a rate constant framework as opposed to a collision kernel, because the latter only applies to a local population, but this analysis is applied to spatially averaged observations of the DSD. Spatial averaging is necessary because of the limited sampling volume of presently available cloud probes. Retrieved rate constants are non-dimensionalized by rate constants derived from a collision–coalescence box model. The resulting enhancement factors evaluate how well existing collision kernels reproduce the observations when applied to spatially averaged DSDs.

The main conclusions of this study are as follows.

- Compared with the quiescent Hall kernel, the rate constant analysis shows that non-unity enhancement factors (EF) are required to explain observed DSDs (Figure 5).
- Leg composite EF values are a decreasing function of collector drop size and range from 0.1 to 40.
- The greatest EF values are found for small monomer cases, suggesting that condensation likely plays a non-trivial role in growing the right tail of the DSD for these cases. The inability of the turbulent collision kernel, which has the greatest effect on small monomer size DSDs, to reduce the EF to order unity supports this interpretation.
- The upper bound of the range of EF is higher for an averaging length of 1.5 km (maximum EF=111). This is likely because leg composite k_0 values were used to derive segment EF (Figure 6).
- There is an order of magnitude or more variability in EF at any drop size. We speculate that this reflects spatial heterogeneity in the DSD.
- EF values decrease for all drop sizes using a turbulent kernel, but, even for a relatively high dissipation rate in stratocumulus ($\epsilon = 30\,\mathrm{cm^2\,s^{-3}}$), most EFs exceed unity and variability remains about an order of magnitude (Figure 7). This suggests that turbulence can account for at most about half of the observed EF.

There are several possible explanations for the magnitude and variability of the enhancement factors. Particularly for EF>1, we have assumed that the monomer diameter is reached by condensation alone. In reality, collision–coalescence may alter the shape of the DSD, such that the monomer diameter in the absence of collision–coalescence is smaller than the observed mode diameter. This effect will be more pronounced for larger mode diameters. Another explanation is that there are missing microphysical processes that can accelerate collisional growth of cloud drops by up to an order of magnitude, which seems unlikely given the significant body of work in this field over the last 80+ years (e.g. Pruppacher and Klett, 1997). The more likely explanation is that applying a collision kernel to a spatially averaged DSD cannot predict DSD evolution accurately, something that has been described previously (Austin *et al.*, 1995; Pincus and Klein, 2000). Of greatest relevance to this work, Pincus and Klein (2000) point out that applying a nonlinear collision–coalescence kernel to a spatially averaged DSD yields a smaller collision–coalescence rate than would be obtained by averaging the rates calculated from local DSDs. This makes physical sense, because drops that are kilometres apart cannot collide within a reasonable time-scale.

One consequence of this result is that models that are too coarse to resolve small-scale variability of the DSD cannot represent collision–coalescence accurately. Our results show that an averaging length-scale of 1.5 km is too coarse, but we are not able to constrain the lower bound of this length-scale, due to sampling limitations. All present-day global and regional climate models, as well as many cloud-resolving models, use resolutions greater than 1 km. Existing upscaling schemes neglect spatial structure and assume a Gaussian distribution of DSD moments (Larson *et al.*, 2002; Larson and Griffin, 2013). Marshak *et al.* (1997) analyze aircraft observations of LWC in stratocumulus, where they find that Gaussian statistics are inadequate to describe all but one of the flights examined. Further work is required to assess whether the inclusion of DSD spatial structure would improve the representation of cloud processes in numerical models significantly.

Finally, this study highlights the need for innovative cloud sampling strategies and instrumentation, as currently available aircraft-mounted cloud probes are faced with a trade-off between statistical significance and physical process relevance, due to a small sampling volume and the inability to sample a Lagrangian air mass. Gerber *et al.* (2013) observed 'cloud

holes' at length-scales of the order of 1 m, while Beals *et al.* (2015) show clustering effects (i.e. deviations from a uniform drop distribution) in instantaneous measurements of a 3D sample volume $V \sim 10\,\mathrm{cm}^3$, illustrating the problematic nature of the concept of a homogeneous drop-size distribution over longer length-scales. Such results also call into question the most common approaches to parametrizing the DSD for bulk microphysical schemes, wherein shape parameters are fitted to *in situ* observations averaged over length-scales of at least 100 m (Geoffroy *et al.*, 2010) or empirical relationships are diagnosed from numerical modelling studies with an explicit microphysics scheme that assumes an homogeneous DSD within each grid cell (Khairoutdinov and Kogan, 2000). To evaluate the idea that a length-scale of 100 m is sufficient for a 'local' description of the DSD as Khain *et al.* (2015) assert, statistically sound observations on length-scales shorter than 100 m are necessary.

5. Data availability

All data used in this manuscript can be obtained freely from https://www.eol.ucar.edu/projects/post/. The MATLAB codes used to process the data and obtain the results presented are available from the corresponding author upon request.

Appendix A: Details of the rate constant analytical framework

The rate constant analysis is composed of five steps.

(1) Aircraft observations are analyzed to identify cloud-top altitude for each leg and subsampled within 40 m of the cloud top for each leg and segment. The closure parameter k_0 is calculated from observations between 40 and 80 m below the cloud top.
(2) The cloud-top DSD is rebinned to linear 'collision space' based on the monomer diameter d_0 and mass m_0, such that drops are regrouped as a linear combination of drops of size m_0.
(3) For context, the collision–coalescence box model of Bott (1998) is run with a known collision kernel and the model DSD is initialized to the shape of the analyzed DSD with which the box model results will be compared.
(4) Observed rate constants are estimated from the rebinned DSDs assuming a steady-state distribution.
(5) Enhancement factors are calculating by dividing observed rate constants by reference rate constants.

Each step is described in more detail below, with appropriate references to descriptions contained in the main text. Unless otherwise noted, leg composite and individual segment DSDs are handled in the same way.

A1. Analysis and subsampling of observations (Step 1)

The cloud top is defined as in section 2.1 and PDI observations are subsampled within 40 m of the cloud top to derive cloud-top DSD, mode diameter d_0, total PDI concentration N_D and rain rate R_CT. The leg composite cloud-top altitude is also used when determining microphysical quantities from individual segments. The closure parameter k_0 used to generate observed rate constants depends on the quantities $\overline{w_\uparrow}$, $f_\uparrow$ and n_0, all of which are derived from leg composite averages sampled from 40 to 80 m below the cloud top.

A2. DSD conversion to linear 'collision space' (Step 2)

Step 2 is explained in section 2.2. The power-law slope β is estimated from the rebinned DSDs. Equation (1) is the basis for this step of the analysis, but because both the PDI and the Bott model use a logarithmic size grid, we must also take into account outcomes of collision events other than the default outcome of advancing a single bin ($\Delta i = 1$). Collisions may also result in a drop remaining in the same bin ($\Delta i = 0$) or advancing two bins ($\Delta i = 2$). Weights $w_{i,\Delta i}$ for each collision outcome and analyzed DSD are calculated based on the PDI distributions within each collision bin and incorporated into Eq. (1):

$$\frac{\mathrm{d}n_i}{\mathrm{d}t} = k_{i-2} w_{i-2,2} n_0 n_{i-2} + k_{i-1} w_{i-1,1} n_0 n_{i-1} - k_i (1 - w_{i,0}) n_0 n_i, \quad \text{(A1)}$$

where the factor of $(1 - w_{i,0})$ in the third term on the right-hand side represents the loss of drops to bin *i+1*, reduced by the fraction of drops that remain in bin *i*. Equation (1) can be recovered by assuming $w_{i-1,1} = 1$ and $w_{i-2,2} = w_{i,0} = 0$. The inclusion of the weighting factors results in an overdetermined linear system. This exact form of Eq. (A1) with weights $w_{i,\Delta i}$ calculated from input DSDs is used to calculate all results presented in the main text, with the left-hand side set equal to 0 for the observed rate constants.

A3. Calculation of reference rate constants (Step 3)

The drop size grid of the Bott model is set to match the PDI lower size bound and bin width ($d_\mathrm{min} = 2.0363\,\mu\mathrm{m}$ and $\mathrm{dlog}_{10}\, d = 0.0156$, respectively), with 200 bins such that the model uses a comparable logarithmic size grid to that of the PDI. The DSD is initialized as a piecewise combination of log-normal and power-law distributions (see section 3.1.1 for a complete description). In addition to the distribution parameters d_0 and β, the total drop concentration N_D is also taken from the observations to initialize the DSD. The model is run for a single time step with $\Delta t = 1\,\mathrm{s}$. We do not run the model for multiple time steps or to the steady state, because we seek a direct transform from kernel values to rate constants. Multiple time steps are redundant, because collision–coalescence is a recursive process and the magnitude of retrieved rate constants is highly sensitive to DSD shape. Therefore reference rate constants must be calculated after every time step or information is lost. The model is not run to steady state because mass begins to accumulate at large drop sizes, which quickly depletes drop mass in the size region of interest unless an unphysical drop removal mechanism is incorporated to preserve the DSD shape or monomer concentration is held constant. Changes in drop concentration as a function of time are known, such that the steady-state assumption is not required.

The Bott model output is then linearly rebinned (i.e. repeat Step 2); recall that the bin spacing of the model output is identical to that of the PDI, such that no modifications are necessary to account for discrepancies between the model and observations in bin spacing or boundaries.

Rate constants are then calculated from model output following a nearly identical procedure to the one that will be applied to the observations: the linear system of equations based on Eq. (A1) is solved with the Bott model output instead of the observed cloud-top DSDs. There are two major differences when solving the linear system with the Bott model output: (i) a steady state is not assumed, because changes in concentration as a function of time are known and (ii) no assumption about the closure parameter k_0 is required, because the change in monomer concentration with time is known, i.e. k_0 is calculated explicitly.

A4. Calculation of observed rate constants and enhancement factors (Steps 4–5)

Observed rate constants from both leg composite and individual segments are calculated using leg composite k_0 values to provide an independent observational constraint on the source term of monomers to the cloud-top layer. The system of equations based on Eq. (A1) is then solved using observed rebinned DSDs as input.

Finally, observed rate constants are divided by Bott model-derived reference rate constants to calculate enhancement factors.

References

Austin P, Wang Y, Pincus R, Kujala V. 1995. Precipitation in stratocumulus clouds: Observational and modelling results. *J. Atmos. Sci.* **52**: 2329–2352. https://doi.org/10.1175/1520-0469(1995)⟨0522329:PISCOA⟩2.0.CO;2.

Ayala O, Grabowski WW, Wang LP. 2007. A hybrid approach for simulating turbulent collisions of hydrodynamically-interacting particles. *J. Comput. Phys.* **225**(1): 51–73. https://doi.org/10.1016/j.jcp.2006.11.016.

Ayala O, Rosa B, Wang LP, Grabowski W. 2008. Effects of turbulence on the geometric collision rate of sedimenting droplets. Part 2: Theory and parametrization. *New J. Phys.* **10**: 075016. http://stacks.iop.org/1367-2630/10/i=7/a=075016.

Baker MB, Latham J. 1979. The evolution of droplet spectra and the rate of production of embryonic raindrops in small cumulus clouds. *J. Atmos. Sci.* **36**: 1612–1615. https://doi.org/10.1175/1520-0469(1979)036⟨1612:TEODSA⟩2.0.CO;2.

Beals MJ, Fugal JP, Shaw RA, Lu J, Spuler SM, Stith JL. 2015. Holographic measurements of inhomogeneous cloud mixing at the centimeter scale. *Science* **350**: 87–90. https://doi.org/10.1126/science.aab0751.

Beard K, Ochs H. 1993. Warm-rain initiation: An overview of microphysical mechanisms. *J. Appl. Meteorol.* **32**: 608–625. https://doi.org/10.1175/1520-0450(1993)032⟨0608:WRIAOO⟩2.0.CO;2.

Blossey P, Bretherton C, Cetrone J, Khairoutdinov M. 2007. Cloud-resolving model simulations of KWAJEX: Model sensitivities and comparisons with satellite and radar observations. *J. Atmos. Sci.* **64**: 1488–1508. https://doi.org/10.1175/JAS3982.1.

Bott A. 1998. A flux method for the numerical solution of the stochastic collection equation. *J. Atmos. Sci.* **55**: 2284–2293. https://doi.org/10.1175/1520-0469(1998)055⟨2284:AFMFTN⟩2.0.CO;2.

Carman JK, Rossiter DL, Khelif D, Jonsson HH, Faloona IC, Chuang PY. 2012. Observational constraints on entrainment and the entrainment interface layer in stratocumulus. *Atmos. Chem. Phys.* **12**: 11 135–11 152. https://doi.org/10.5194/acp-12-11135-2012.

Chuang PY, Saw EW, Small JD, Shaw RA, Sipperley CM, Payne GA, Bachalo WD. 2008. Airborne phase Doppler interferometry for cloud microphysical measurements. *Aerosol Sci. Technol.* **42**: 685–703. https://doi.org/10.1080/02786820802232956.

Cooper WA, Lasher-Trapp SG, Blyth AM. 2013. The influence of entrainment and mixing on the initial formation of rain in a warm cumulus cloud. *J. Atmos. Sci.* **70**: 1727–1743. https://doi.org/10.1175/JAS-D-12-0128.1.

Davis MH. 1972. Collisions of small cloud droplets: Gas kinetic effects. *J. Atmos. Sci.* **29**: 911–915. https://doi.org/10.1175/1520-0469(1972)029⟨0911:COSCDG⟩2.0.CO;2.

Geoffroy O, Brenguier JL, Burnet F. 2010. Parametric representation of the cloud droplet spectra for LES warm bulk microphysical schemes. *Atmos. Chem. Phys.* **10**: 4835–4848. https://doi.org/10.5194/acp-10-4835-2010.

Gerber H, Frick G, Malinowski SP, Jonsson H, Khelif D, Krueger SK. 2013. Entrainment rates and microphysics in POST stratocumulus. *J. Geophys. Res. Atmos.* **118**: 12 094–12 109. https://doi.org/10.1002/jgrd.50878.

Haarsma RJ, Roberts M, Vidale PL, Senior CA, Bellucci A, Bao Q, Chang P, Corti S, Fuckar NS, Guemas V, von Hardenberg J, Hazeleger W, Kodama C, Koenigk T, Leung LR, Lu J, Luo JJ, Mao J, Mizielinski MS, Mizuta R, Nobre P, Satoh M, Scoccimarro E, Semmler T, Small J, von Storch JS. 2016. High Resolution Model Intercomparison Project (HighResMIP v1.0) for CMIP6. *Geosci. Model Dev.* **9**: 4185–4208. https://doi.org/10.5194/gmd-9-4185-2016.

Hall W. 1980. A detailed microphysical model within a two-dimensional dynamic framework: Model description and preliminary results. *J. Atmos. Sci.* **37**: 2486–2507. https://doi.org/10.1175/1520-0469(1980)037⟨2486:ADMMWA⟩2.0.CO;2.

Hocking LM, Jonas PR. 1970. The collision efficiency of small drops. *Q. J. R. Meteorol. Soc.* **96**: 722–729. https://doi.org/10.1002/qj.49709641013.

Igel AL, van den Heever SC. 2017. The importance of the shape of cloud droplet size distributions in shallow cumulus clouds. Part I: Bin microphysics simulations. *J. Atmos. Sci.* **74**: 249–258. https://doi.org/10.1175/JAS-D-15-0382.1.

Jensen JB, Lee S. 2008. Giant sea-salt aerosols and warm rain formation in marine stratocumulus. *J. Atmos. Sci.* **65**: 3678–3694. https://doi.org/10.1175/2008JAS2617.1.

Johnson DB. 1982. The role of giant and ultragiant aerosol particles in warm rain initiation. *J. Atmos. Sci.* **39**: 448–460. https://doi.org/10.1175/1520-0469(1982)039⟨0448:TROGAU⟩2.0.CO;2.

Jonas P. 1972. The collision efficiency of small drops. *Q. J. R. Meteorol. Soc.* **98**: 681–683. https://doi.org/10.1002/qj.49709841717.

Khain AP, Beheng KD, Heymsfield A, Korolev A, Krichak SO, Levin Z, Pinsky M, Philips V, Prabhakaran T, Teller A, van den Heever SC, Yano JI. 2015. Representation of microphysical processes in cloud-resolving models: Spectral (bin) microphysics versus bulk parametrization. *Rev. Geophys.* **53**: 247–322. https://doi.org/10.1002/2014RG000468.

Khairoutdinov M, Kogan Y. 2000. A new cloud physics parametrization in a large-eddy simulation model of marine stratocumulus. *Mon. Weather Rev.* **128**: 229–243. https://doi.org/10.1175/1520-0493(2000)128⟨0229:ANCPPI⟩2.0.CO;2.

Klett J, Davis M. 1973. Theoretical collision efficiencies of cloud droplets at small Reynolds numbers. *J. Atmos. Sci.* **30**: 107–117. https://doi.org/10.1175/1520-0469(1973)030⟨0107:TCEOCD⟩2.0.CO;2.

Larson VE, Griffin BM. 2013. Analytic upscaling of a local microphysics scheme. Part I: Derivation. *Q. J. R. Meteorol. Soc.* **139**: 46–57. https://doi.org/10.1002/qj.1967.

Larson V, Golaz JC, Cotton WR. 2002. Small-scale and mesoscale variability in cloudy boundary layers: Joint probability density functions. *J. Atmos. Sci.* **59**: 3519–3539. https://doi.org/10.1175/1520-0469(2002)059⟨3519:SSAMVI⟩2.0.CO;2.

Lau K, Wu H. 2003. Warm rain processes over tropical oceans and climate implications. *Geophys. Res. Lett.* **30**: 2290. https://doi.org/10.1029/2003GL018567.

Lin C, Lee S. 1975. Collision efficiency of water drops in the atmosphere. *J. Atmos. Sci.* **32**: 1412–1418.

de Lozar A, Muessle L. 2016. Long-resident droplets at the stratocumulus top. *Atmos. Chem. Phys.* **16**: 6563–6576. https://doi.org/10.5194/acp-16-6563-2016.

Malinowski SP, Gerber H, Jen-La Plante I, Kopec MK, Kumala W, Nurowska K, Chuang PY, Khelif D, Haman KE. 2013. Physics of Stratocumulus Top (POST): Turbulent mixing across capping inversion. *Atmos. Chem. Phys.* **13**: 12 171–12 186. https://doi.org/10.5194/acp-13-12171-2013.

Marshak A, Davis A, Wiscombe W, Cahalan R. 1997. Scale invariance in liquid water distributions in marine stratocumulus. Part II: Multifractal properties and intermittency issues. *J. Atmos. Sci.* **52**: 1423–1444. https://doi.org/10.1175/1520-0469(1997)054⟨1423:SIILWD⟩2.0.CO;2.

Medeiros B, Stevens B, Held IM, Zhao M, Williamson DL, Olson JG, Bretherton CS. 2008. Aquaplanets, climate sensitivity and low clouds. *J. Clim.* **21**: 4971–4991. https://doi.org/10.1175/2008JCLI1995.1.

Morrison H, Gettelman A. 2008. A new two-moment bulk stratiform cloud microphysics scheme in the Community Atmosphere Model, Version 3 (CAM3). Part I: Description and numerical tests. *J. Clim.* **21**: 3642–3659. https://doi.org/10.1175/2008JCLI2105.1.

Pincus R, Klein SA. 2000. Unresolved spatial variability and microphysical process rates in large-scale models. *J. Geophys. Res.* **105**: 27 059–27 065. https://doi.org/10.1029/2000JD900504.

Pruppacher H, Klett J. 2010. *Microphysics of Clouds and Precipitation*. Springer: Dordrecht, Netherlands. https://doi.org/10.1007/978-0-306-48100-0.

Reiche CH, Lasher-Trapp S. 2010. The minor importance of giant aerosol to precipitation development within small trade wind cumuli observed during RICO. *Atmos. Res.* **95**: 386–399. https://doi.org/10.1016/j.atmosres.2009.11.002.

Rossiter DL. 2012. 'Observational studies of drizzle in marine stratocumulus', PhD thesis. University of California: Santa Cruz, CA.

Shafrir U, Gal-Chen T. 1971. A numerical study of the collision efficiencies and coalescence parameters for droplet pairs with radii up to 300 microns. *J. Atmos. Sci.* **28**: 741–751. https://doi.org/10.1175/1520-0469(1971)028⟨0741:ANSOCE⟩2.0.CO;2.

Siebert H, Shaw R, Warhaft Z. 2010. Statistics of small-scale velocity fluctuations and internal intermittency in marine stratocumulus clouds. *J. Atmos. Sci.* **67**: 262–273. https://doi.org/10.1175/2009JAS3200.1.

Slingo A. 1990. Sensitivity of the Earth's radiation budget to changes in low clouds. *Nature* **343**: 49–51. https://doi.org/10.1038/343049a0.

Stevens B, Lenschow DH, Vali G, Gerber H, Bandy A, Blomquist B, Brenguier JL, Bretherton CS, Burnet F, Campos T, Chai S, Faloona I, Friesen D, Haimov S, Laursen K, Lilly DK, Loehrer SM, Malinowski SP, Morley B, Petters MD, Rogers DC, Russell L, Savic-Jovcic V, Snider JR, Straub D, Szumowski MJ, Takagi H, Thornton DC, Tschudi M, Twohy C, Wetzel M, van Zanten MC. 2003. Dynamics and chemistry of marine stratocumulus – DYCOMS-II. *Bull. Am. Meteorol. Soc.* **84**: 579–593. https://doi.org/10.1175/BAMS-84-5-579.

Vali G, Kelly RD, French J, Haimov S, Leon D, McIntosh RE, Pazmany A. 1998. Finescale structure and microphysics of coastal stratus. *J. Atmos. Sci.* **55**: 3540–3564. https://doi.org/10.1175/1520-0469(1998)055⟨3540:FSAMOC⟩2.0.CO;2.

Wang LP, Grabowski W. 2009. The role of air turbulence in warm rain initiation. *Atmos. Sci. Lett.* **10**: 1–8. https://doi.org/10.1002/asl.210.

Wood R. 2012. Stratocumulus clouds. *Mon. Weather Rev.* **140**: 2373–2423. https://doi.org/10.1175/MWR-D-11-00121.1.

Wood R, Kubar TL, Hartmann DL. 2009. Understanding the importance of microphysics and macrophysics for warm rain in marine low clouds. Part II: Heuristic models of rain formation. *J. Atmos. Sci.* **66**: 2973–2990. https://doi.org/10.1175/2009JAS3072.1.

Wyszogrodzki AA, Grabowski WW, Wang LP, Ayala O. 2013. Turbulent collision–coalescence in maritime shallow convection. *Atmos. Chem. Phys.* **13**: 8471–8487. https://doi.org/10.5194/acp-13-8471-2013.

